

## Research Article

# Design and Application of Blasting Parameters for Presplitting Hard Roof with the Aid of Empty-Hole Effect

Baobao Chen <sup>1,2</sup>, Changyou Liu <sup>1,2</sup> and Jingxuan Yang <sup>1,2</sup>

<sup>1</sup>Key Laboratory of Deep Coal Resource Mining, Ministry of Education of China, School of Mines, China University of Mining and Technology, Xuzhou 221116, China

<sup>2</sup>State Key Laboratory of Coal Resource and Mine Safety, Xuzhou 221116, China

Correspondence should be addressed to Changyou Liu; [lcycumt@cumt.edu.cn](mailto:lcycumt@cumt.edu.cn) and Jingxuan Yang; [jxyang@cumt.edu.cn](mailto:jxyang@cumt.edu.cn)

Received 14 March 2018; Revised 24 May 2018; Accepted 2 July 2018; Published 2 September 2018

Academic Editor: Salvatore Russo

Copyright © 2018 Baobao Chen et al. This is an open access article distributed under the Creative Commons Attribution License, which permits unrestricted use, distribution, and reproduction in any medium, provided the original work is properly cited.

Theoretical calculation and numerical simulation were performed to analyze the mechanism of rock fracturing between holes in deep-hole presplit blasting, crack evolution under the synergistic action of dynamic and static loads, and the mechanism of fracture movement guided by tangential stress concentration of empty holes. The pattern and characteristic zones of main and wing cracks across a cross section were identified. Combined with blast dynamics, the scope of stress-induced cracks around blast holes and the maximum length of secondary cracks induced by detonation gas was calculated. It was found that the initiation and extension of cracks were oriented predominantly along the line passing through the hole centers (LPTHC). Moreover, the maximum length of the tensile crack zone induced by reflected stress waves was obtained. The effects of empty-hole diameter and charge coefficient on crack propagation were analyzed, and the proper blast-hole spacing was determined. Later, a LS-DYNA<sup>3D</sup> blast model was used to illustrate von Mises stress propagation, strain variation, and evolution of main and wing cracks between holes. The scope of strain failure, fracture pattern, and crack characteristic zones in the rock mass was determined. The results demonstrate that the hole spacing, at 3.2 m, is reasonable. Furthermore, blasting parameters were determined for 8939 working face at Xinzhouyao Mine and then deep-hole blasting was implemented to presplit the hard roof. After presplitting, the working resistance of supports was significantly reduced, thereby achieving effective control on the hard roof.

## 1. Introduction

Drill blasting is the most common way to break rock masses in mines, as it is adaptable to various geological conditions and cost effective and involves a relatively simple procedure. When used for breaking hard rock, conventional blasting techniques can hardly deliver desired results due to their limitations and increased operational difficulty. Radial compression and tangential tension that arise from stress waves are the major driving forces for the cracking of a blasted rock mass [1]. During large-scale blasting of rocks in deep underground, however, there is limited space to allow for free movement of rock. To solve this problem, we propose using large diameter empty holes to provide sufficient space for rock movement [2, 3]. The empty holes were

found to be able to enhance the effectiveness of presplit blasting by improving the distribution of tensile stress in the surrounding rock and guiding the initiation and growth of cracks [4].

The presence of empty holes in the rock mass can alter stress distribution and cause stress concentration [5], thereby guiding crack propagation. Empty holes have been successfully applied to rock presplitting for unloading, blasting excavation of rock drift, and gas extraction from gas-rich coalbeds [6–8]. There have been extensive studies on investigating the mechanism of the dynamic behavior for blasting crack propagation as well as the tension crack and guiding role of empty holes, which are mainly based on experimental and theoretical analysis. Arkawa and Mada [9] studied the effects of specimen dimensions on the pattern

and propagation rate of main cracks under different loading conditions through experiments on polymeric methyl methacrylate (PMMA) plate specimens. Based on the characteristics of crack evolution between holes, Mohanty [3] examined the feasibility of designing an empty hole at the midpoint between the centers of adjacent holes to guide crack propagation. Using dynamic analysis software LS-DYNA, Wang and Konietzky [10] simulated the stress and crack evolution in an infinite rock mass with a single free face during blasting. The results can provide a basis for research on techniques that use free surface to guide fracture formation. Yang et al. [11, 12] simulated the superposition of stress waves around the empty holes and the tension caused by reflected waves with LS-DYNA. By the dynamic photoelastic method and the digital laser dynamic caustics experimental system, Malezhik et al. [13] analyzed the crack evolution between holes and dynamic stress intensity factors surrounding the crack tip and revealed the effects of hole spacing and shape of empty hole on the propagation rate and direction of cracks. Based on an analysis on the influence of empty holes on main crack path, Yue et al. [14] and Yang and Wang [15] discovered how the main crack propagation rate and strain field around empty holes responded to changes in empty-hole diameter. To study the influence of hole shape on crack initiation and propagation, Cho et al. [16] and Nakamura et al. [17] conducted a comparative analysis on the main crack propagation rates and dynamic stress intensity factor evolution for specimens with ordinary empty holes and with notched holes of different shapes.

Most of these studies focused on the propagation rate of main cracks and the effects of empty-hole shape and hole spacing on blasting results. The research on fracture development was mostly based on comparison between element stress and rock strength at failure, rather than modeling of fracture evolution in a real sense. Moreover, because existing studies of cracks near empty holes were mostly concentrated on fracture pattern, there is a lack of research into the dynamics of complex fracture pattern and quantitative effect of hole diameter on fracture-moving. In the present study, theoretical analysis and numerical simulation were performed to analyze the stress concentration around an empty hole and tension caused by reflected stress waves and to calculate the lengths of initial and secondary cracks around a blast hole. The relationship between empty-hole diameter and length of cracks guided by empty holes was quantified. The blasting parameters and hole spacing were optimized. Moreover, the study illustrated the dynamic evolution of the strain and the complex fracture network in a blasted rock mass under the synergistic action of dynamic and static loads. The findings are expected to provide guidance on deep-hole presplit blasting for breaking rocks.

## 2. Mechanism of Fracturing by Blasting

After deep-hole blasting of a rock mass, the resulting stress near a blast hole exceeds the rock's dynamic compressive strength. This, combined with the high strain rate, will create a crushed zone. This process can consume the majority of the energy released by blasting. Meanwhile, the stress waves

decay into compression waves along the boundary of the crushed zone and the reverse stress relief produces a tangential force, which then induces radial cracks. As wing cracks develop, the main and wing cracks will form an initial concentric fracture network (fractured zone, Stage I) [18, 19].

After initial cracks' formation, the products of detonation fill space in the fracture network and exert quasi-static loads on fracture tips, leading to secondary fracture extension (fractured zone, Stage II). At the same time, the stress waves reflected from the free surface of empty hole induce tensile stress and thus stimulate the formation and transfixion of complex fractures including the tensile main cracks and annular wing cracks. The complex fractures then interconnect with the cracks induced by detonation gas to form the presplitting cracks and a fracture network between blasting holes. Figure 1 shows the schematic of the characteristic crack zones.

*2.1. Mechanism of Fracturing Induced by Stress Waves.* Combined with the charge structure of deep-hole presplitting blast for rock mass, the cylindrical explosive charge is employed for calculating the overpressure induced by blasting stress waves impacting on the holes' wall. The peak intensity,  $P_m$ , is given by the below equation [20]:

$$P_m = \frac{2\rho D_p}{\rho_0 D_0 + \rho D_p} n_0 \frac{\rho_0 D_0^2}{8} k_r^{-2\gamma} l_c^{-1}, \quad (1)$$

where  $\rho$  is the rock density;  $D_p$  is the longitudinal wave velocity of rock;  $\rho_0$  is the explosive density;  $D_0$  is the velocity of explosive;  $n_0$  is the stress intensification factor;  $k_r = r_c/r_b$ ,  $r_c$ ,  $r_b$  are the radii of the blast hole and explosive, respectively;  $\gamma$  is the thermal insulation factor of the explosive, 3; and  $l_c$  is the axial decoupling charge coefficient. Combined with (1),  $P_m$  mainly depends on the physical and mechanical parameters of coal and rock and the structure of explosive charge.

Combined with the stress intensity coefficient  $C$  of rock blasting, the radius of crushing zone  $R_c$  is obtained [21]:

$$C = \sqrt{(1+b)^2 - 2\mu_d(1-b)^2(1-\mu_d) + (1+b^2)}, \quad (2)$$

$$R_c = \left( P_m \frac{C}{\sqrt{2}} \frac{1}{\sigma_c \xi^{1/3}} \right)^{1/\alpha} r_b,$$

where  $b$  is the side pressure coefficient;  $\mu_d$  is the dynamical Poisson ratio;  $\sigma_c$  is the static uniaxial compressive strength;  $\xi$  is the loading strain rate;  $\alpha$  is the shock wave attenuation coefficient,  $2+b$ ; and  $\beta$  is the stress wave attenuation coefficient,  $2-b$ . Considering the three-dimensional stress of blasted rock in the crushed zone, the radius of the crushing zone depends on the charge structure and the dynamic mechanical parameters of the rock mass.

The rock mass is in a critical state along the boundary of the crushed zone, which represents the interface between compression failure and tensile failure, with  $\sigma_m = (\sqrt{2}\xi^{1/3}\sigma_c/C)$ . The radius of the initial crack zone,  $R_p$ , can be described by the equation below [20]:

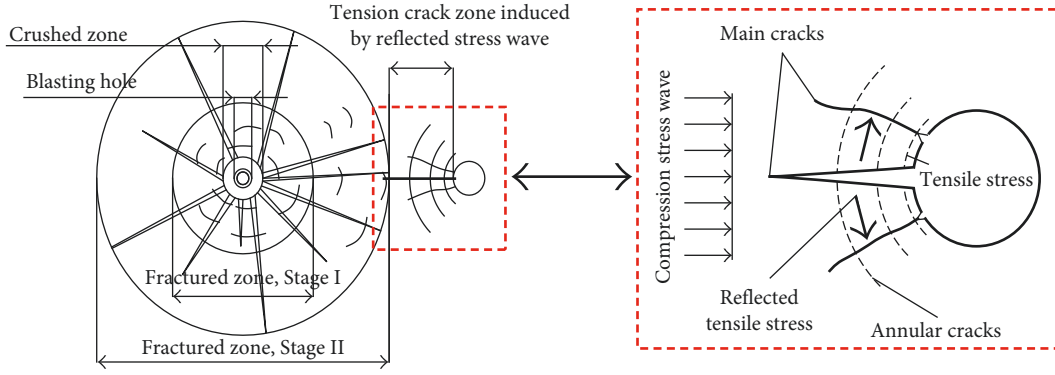


FIGURE 1: Fracture development characteristics of rock mass with empty holes induced by blasting loading.

$$R_p = \left[ \left( \frac{C\sigma_m}{\sqrt{2}(\sigma_{td} + \sigma_h)} \right)^{1/\beta} - 1 \right] \cdot \left[ P_m \frac{C}{\sqrt{2}} \frac{1}{\sigma_c \xi^{1/3}} \right]^{1/\alpha} \cdot r_c, \quad (3)$$

where  $\sigma_{td}$  is the dynamic tensile strength of rock and  $\sigma_h$  is the rock stress.  $R_p$  (fractured zone, Stage I) mainly depends on  $\sigma_m$  and  $\sigma_h$ , and meanwhile,  $\sigma_m$  mainly depends on the charge structure of explosives. Therefore, the research emphasizes on  $R_c + R_p$  in the presplitting blasting, which is the charge structure coefficient.

**2.2. Mechanism of Crack Propagation Driven by Detonation Gas.** The cracks induced by detonation gas initiate at initial cracks. The diffusion of detonation gas is quasi-static and uniform. After the gas reaches a crack tip, it will cause tensile failure and stimulate further growth of the crack, resulting in secondary cracks [22].

As the secondary propagation of initial cracks driven by detonation gas continues, pressure drop occurs. When the pressure declines to a critical value needed for brittle failure of the rock, the secondary crack propagation stops [23, 24].

The relationship between the fracturing length induced by the detonation gas and the crack propagating critical stress  $\sigma_{cl}$  could be obtained as follows [25]:

$$\sigma_{cl} = \frac{K_{IC}}{\sqrt{2\pi(R_c + R_p + l_k)}}, \quad (4)$$

where  $l_k$  is the cracking length induced by detonation gas and  $K_{IC}$  is the fracturing tenacity of rock at critical development of Type I.  $K_{IC}$  represents the ability of the rock mass preventing crack propagation and is the critical value of the stress intensity factor, which is a constant under quasi-static loading. When the initial crack size is determined, the larger the fracture toughness of the rock mass is, the greater the critical stress needed for the crack propagation is. Therefore, the critical propagation stress of detonation gas fracturing is mainly determined by  $R_c + R_p$ . For  $R_c$  being much smaller than  $R_p$ , it is employed as a part of total crack length on calculating  $\sigma_{cl}$ .

$K_{IC}$  can be experimentally measured. It is given by

$$K_{IC} = \alpha_k \frac{P_{\min}}{t_h \sqrt{D_1/2}}, \quad (5)$$

where  $P_{\min}$  is the first minimum that occurs after the peak tensile strength measured by the Brazilian test,  $D_1$  is the specimen diameter,  $t_h$  is the specimen thickness, and  $\alpha_k$  is the dimensionless intensity attenuation coefficient. During the loading process of the flattened Brazilian disc, the loading variation with the length of the dimensionless crack corresponds to the variation of  $\alpha_k$ , and moreover, the maximum value of  $\alpha_k$  is exactly corresponding to the load dropping from the maximum to the first minimum in the load-displacement curve. At that moment, the critical length of the cracks would be at the maximum,  $\alpha_k = 0.8$  [26].

Since the detonation gas is confined within the fracture network, its transient pressure during isentropic expansion,  $p_x$ , can be written as follows:

$$p_x = p_c \left[ \frac{V_c}{V} \right]^{\gamma+1} = \sigma_{cl} \left[ 1 + \frac{mnu \cdot (l_x + 2R_p + 2R_c)}{\pi(r_c + R_c)^2} \right]^{\gamma+1}, \quad (6)$$

where  $n$  is the number of main cracks,  $m$  is the interconnected enlarging coefficient of main and wing cracks, and  $u$  is the maximum aperture of the single fracture in the crushing zone border line.

The angle between the two fracture-extended surfaces at the fracture tip is set at zero here and given that it is very small. Then, the maximum fracture opening  $u$  can be obtained based on the quasi-static propagation of a single main crack as follows (Figure 2) [1, 25]:

$$u = \frac{K_{IC}}{2G} \sqrt{\frac{R_p + l_k}{2\pi \cos(\theta/2)}} \left( \gamma + \cos \frac{\theta}{2} \right) \cdot \cos \frac{\theta}{4} \approx \frac{K_{IC}}{2G} \sqrt{\frac{R_p + l_k}{2\pi}} (\gamma + 1), \quad (7)$$

where  $\theta$  is the tip angle of cracks and  $G$  is the shear modulus.  $u$  mainly depends on the radius of primary crack and the length of secondary cracks induced by detonation gas.

The relationship between the maximum length of secondary cracks induced by detonation gas, denoted  $l_{k(\max)}$ , and detonation pressure  $p_x$  was derived based on (4) through (8). It can be written in the following form:

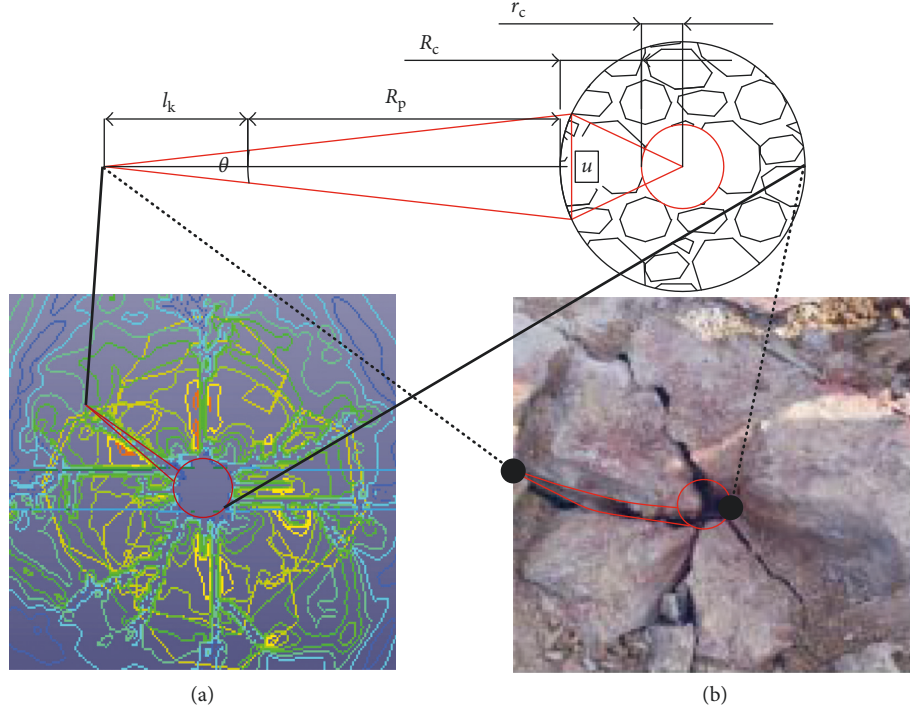


FIGURE 2: Plan view of the tip of a single initial crack. (a) Numerical simulation. (b) Field measurement.

$$\left( \frac{P_x \sqrt{2\pi(R_c + R_p + l_{k(\max)})}}{K_{IC}} \right)^{1/\gamma+1} - \frac{mn(\alpha_k(P_{\min}/t_h \sqrt{D_l/2})) \sqrt{(R_p + l_{k(\max)})} (k+1)(2R_c + 2R_p + l_{k(\max)})}{2\sqrt{2\pi}G\pi(R_c + r_c)^2} - 1 = 0. \quad (8)$$

As (8) shows, the crack propagating length is negatively correlated with the critical pressure of detonating gas during the cracking process induced by detonating gas, and therefore, only the higher pressure in the early detonation gas can produce more number of main cracks in the rock mass. For the specific number of main cracks,  $l_k$  increases with the rise of the detonation gas pressure, and consequently,  $l_{k(\max)}$  can be obtained by determining the maximum pressure at the extending initial stage of the detonation gas.

Therefore, the crack zone near a blast hole is the product of the initial fracture induced by the stress wave combined with the  $(R_c + R_p)$  secondary fracture driven by detonation gas.

**2.3. Mechanism of Fracturing Guided by Empty Holes.** After an empty hole is drilled in a rock mass, the stress near the hole is redistributed and the stress waves reflected from the free surface lead to stress concentration, which then drives crack initiation and propagation. Stress evolution of the rock mass along the line passing through the hole centers (LPTHC) is shown in Figure 3 [27].

In the figure above,  $\sigma_{\rho\rho}$  and  $\sigma_{\varphi\varphi}$  are the radial and tangential stresses, respectively, in the rock surrounding an empty hole;  $\sigma_\rho$  and  $\sigma_\varphi$  represent the blast-induced radial and tangential stresses, respectively;  $\varphi$  is the angle between the line segments connecting the rock element and the line

through centers of two adjacent holes; and  $k_0$  is the in situ stress concentration factor.

Combining with stress concentration near circular hole in elastic mechanics, the stress distribution around the empty holes in an infinite plane is obtained as follows [28]:

$$\begin{aligned} \sigma_{\rho\rho} &= \frac{\sigma_\varphi - \sigma_\rho + \sigma_h}{2} (1 - k^2) + \frac{\sigma_\varphi + \sigma_\rho + \sigma_h}{2} \\ &\quad \cdot \cos 2\varphi (1 - k^2) (1 - 3k^2), \\ \sigma_{\varphi\varphi} &= \frac{\sigma_\varphi - \sigma_h - \sigma_\rho}{2} (1 + k^2) + \frac{\sigma_\varphi - \sigma_h + \sigma_\rho}{2} \cos 2\varphi (1 + 3k^4), \end{aligned} \quad (9)$$

where  $r$  represents the straight-line distance between a point in the surrounding rock and the empty-hole center and  $r_k$  is the radius of empty hole,  $k = r_k/r$ . According to the characteristics of  $\sigma_{\rho\rho}$  and  $\sigma_{\varphi\varphi}$  distribution around the guiding hole, it could be found that the values of  $\sigma_{\rho\rho}$  and  $\sigma_{\varphi\varphi}$  are inversely proportional to its distance from the empty hole; that is, the stress concentration effect of the empty hole is reduced with  $r$  increasing. It shows that the stress concentration effect only occurs in the local.

Let  $m = \sigma_h/\sigma_\rho$ . Then, the relationships between stress concentration factor (SCF,  $SCF = \sigma_{\varphi\varphi}/\sigma_\rho$ ) and  $\varphi$  for different  $k$  values can be obtained using (9) (Figure 4).

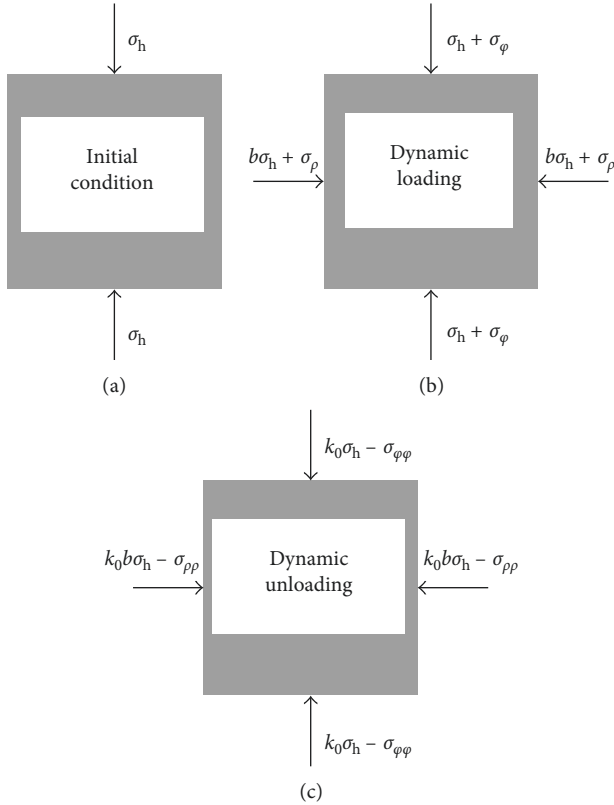


FIGURE 3: Dynamics of stress in a rock element along the LPTHC.

The figure above demonstrates that SCF is symmetrically distributed about the LPTHC and decreases gradually from this line outward. The peak values and maximum stress gradients are located along the axis of symmetry, indicating that the LPTHC represent the dominant crack orientation. Cracking along this line can lead to the maximum length of tensile crack,  $l_{t(max)}$ . Moreover, the SCF along this line decreases with increasing  $k$  at a slower rate, implying that the cracks occur within a certain radius of each empty hole.

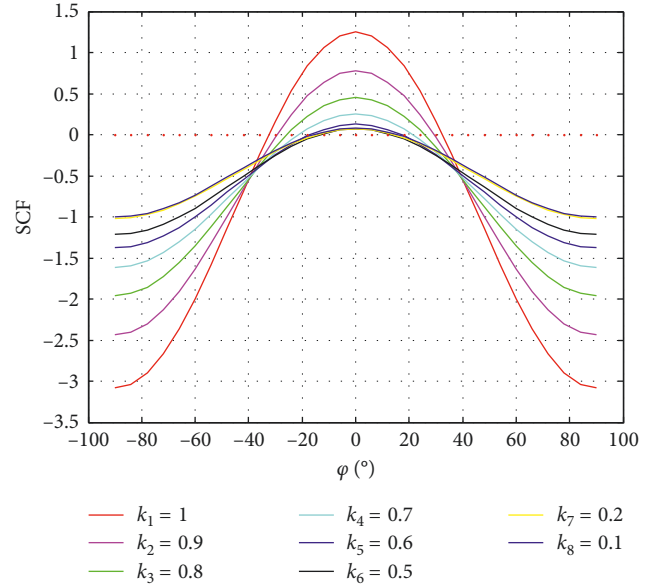
Let the sum of the tensile strength measured under unidirectional tension at a low strain rate and  $\sigma_h$  represent the critical stress needed for cracking guided by empty holes. Then,  $k$  and  $l_{t(max)}$  can be related by the following equation:

$$\sigma_{tm} = C\sigma_{cd} \left( \frac{R_c + R_p + l_{k(max)} + l_{t(max)}}{R_c + R_p + l_{k(max)}} \right)^{-\beta},$$

$$\left[ (1 + \delta) \frac{b-1}{2} \sigma_{tm} - \frac{\sigma_h}{2} \right] (1 + k^2)$$

$$+ \left[ (1 + \delta) \frac{b+1}{2} \sigma_{tm} - \frac{\sigma_h}{2} \right] (1 + 3k^4) \geq (1 - D)\sigma_t, \quad (10)$$

where  $\sigma_{tm}$  is the radial tensile stress produced by reflected stress waves;  $\delta$  is the coefficient of superposition of stress waves, 0.1; and  $D$  is the factor of initial damage to the rock caused by the compression waves. Equation (10) shows the propagation and attenuation characteristics of blasting stress wave reflected from

FIGURE 4: SCF curves for the rock near an empty hole ( $m_0 = 0.25$ ).

the free surface of the guide hole with the fracture length expanding. Combined with the stress concentration effect on LPTHC, the maximum length of tensile crack induced by the reflected tensile stress on the LPTHC can be obtained.

### 3. Simulation and Analysis of Blasting Fracture Parameters

Numerical simulation of the blasting process plays a significant role in the analysis of blasting mechanics. LS-DYNA3D as one of the most effective methods is employed to analyze the nonlinear dynamic questions, including stress propagation and crack evolution characteristics, for exploring the deep-hole presplit cracking mechanism with empty hole.

**3.1. Numerical Model and Constitutive Equation.** According to the field construction and some related contemporary research results, the numerical model and field experiment adopted the Class-2 coal mine permissible emulsion explosive [19, 29]. The JWL state equation is used for describing the relationship between the relative volume  $V$  and pressure of the high-energy explosive detonation gas  $P$  (11) in the LS-DYNA<sup>3D</sup> model. The explosive parameters and JWL equation parameters are listed in Table 1 [30]:

$$P = A \left( 1 - \frac{\omega}{R_1 V} \right) e^{R_1 V} + B \left( 1 - \frac{\omega}{R_2 V} \right) e^{R_2 V} + \frac{\omega E}{V}, \quad (11)$$

where  $A, B, R_1, R_2,$  and  $\omega$  are the material property parameters determined by blasting measurements.  $E_0$  is the initial internal energy of detonation gas.

This study used MAT-PLASTIC KINEMATIC HARDENING as the element material for rock modeling. The rock mass strain was high near the explosive detonation center, and it was proper to use a plastic hardening material model, which included the strain rate effect. Therefore, the

TABLE 1: Explosive parameters.

$\rho_0$ (kg/m <sup>3</sup> )	$D_0$ (m/s)	Equation of state parameter					
		$A$ (GPa)	$B$ (GPa)	$R_1$	$R_2$	$\omega$	$E_0$ (GPa)
1200	3200	322	3.95	4.15	0.96	0.33	4.192

MAT-PLASTIC KINEMATIC was an anisotropy kinematic hardening and isotropic kinematic hardening mixed model, relevant with the strain rate and also considered the material failure effect. During simulation of fracture development, MAT\_ADD\_EROSION was used as the criterion to identify whether an element was dead or alive. As rock mass is subjected to compressive and tensile stresses in three directions during blasting, it was modeled with the Cowper–Symonds high strain rate model [31]:

$$\sigma_y = \left[ 1 + \left( \frac{\dot{\xi}}{c} \right)^{1/p} \right] (\sigma_0 + \beta E_p \xi_p^{\text{eff}}), \quad (12)$$

where  $\sigma_0$  is the initial yield stress;  $c$  and  $p$  are the Cowper–Symonds strain rates, respectively;  $\xi_p^{\text{eff}}$  is the effective plastic strain; and  $E_p$  is the hardening modulus. The hardening parameters  $\beta$  can be varied ( $\beta=0$  means only kinematic hardening,  $0 < \beta < 1$  means mixed hardening, and  $\beta = 1$  means only isotropic hardening) to adjust the isotropic hardening degree and the kinematic hardening degree. Combined with Xinzhouyao Coal Mine, the rock mechanical parameters are shown in Table 2.

The failure of rock mass is mainly determined by element stress and strain. The stress indices mainly consider the four criteria of stress and strain [31], which is shown in Table 3.

Based on the field conditions and theoretical calculation, the LS-DYNA<sup>3D</sup> model was established, with an effective blasting hole spacing of 3.2 m. The geometry size of the model was length  $\times$  width  $\times$  height = 6.4 m  $\times$  15.0 m  $\times$  4.0 m, the cartridge diameter was 40 mm, and the borehole axial depth penetrated the whole model with 15.0 m long charge. Therefore, combined with  $k_r$  and explosive density  $\rho_0$ , explosive charge in per hole could be determined. The guide hole was placed in the center of the whole model, and meanwhile, the guide hole and the blasting hole with the spacing of 1.6 m were alternately built along the model length direction. The model geometry and borehole layout are shown in Figure 5.

Modeling and grid meshing were all based on Cartesian, and the grid near the blasting hole is shown in Figure 6. In the center of the model, the cylinder of diameter 50 mm (explosive) and 0.1 m  $\times$  0.1 m rectangle (rock) were used for refining the grid. The grid of the explosive and the rock were homogenized by “Mapped”. The average size of the explosive element was 3.2 mm. The minimum and maximum sizes of the rock elements were 3.3 mm and 8.3 mm, with the spacing ratio of adjacent elements being 1.17. Combining with the comparison between grid size and fracture opening of rock mass in site, grid meshing of rock was fine enough to accurately simulate the engineering problem on blasting presplitting.

In order to avoid the problem of calculation interruption and simulation accuracy induced by the serious distortion of Lagrange element meshing during the blasting process, the

partition of rock mass and explosive in the modeling is all meshed with Euler, and the multimaterial ALE algorithm is used, that is, allowing a grid to include rock mass and explosive detonation products, for analyzing element deformation and explosive detonation products diffusion. In the process of simulation, the gravity effect of rock mass is ignored. To eliminate the influence of stress reflection and stress concentration on border, nonreflection boundary constraints were applied.

**3.2. Calculation of Blasting Parameters.** Given the synergistic effects of different driving forces, combining with the fracture features zone shown in Figure 1, the hole spacing  $L$  could be decomposed into four components,  $R_c$ ,  $R_p$ ,  $l_{t(\max)}$ , and  $l_{k(\max)}$ :

$$L = 2l_0 = 2(R_c + R_p + l_{k(\max)} + l_{t(\max)}). \quad (13)$$

Equations (1), (3), and (10) suggest that  $R_p$  and  $l_{k(\max)}$  depend largely on  $k_r$ , while  $l_{t(\max)}$  is determined mainly by  $k_r$  and  $r_k$ . It follows that  $k_r$  and  $r_k$  should be the key considerations in research on blasting parameters.

**3.2.1. Radius of Crack Zone near a Blast Hole.** Based on the charge diameter ( $\Phi 40$  mm), the effects of  $k_r$  (1, 1.11, 1.25, 1.5, and 1.875) on the number of main cracks and maximum radius of initial crack zone were analyzed by changing the blast-hole diameter. Figure 7 illustrates how the two characteristic crack parameters respond to the change in  $k_r$ .

As shown in Figure 7, the length and number ( $n$ ) of main cracks are negatively correlated with  $k_r$  and each has an inflection point at  $k_r$  of 1.25. When  $k_r \leq 1.25$ , the number and length of main cracks slightly decrease as  $k_r$  increases. When  $k_r > 1.25$ , the stress waves generated by detonation sharply attenuate in energy with increasing  $k_r$ , and the number and length of main cracks trend approximately linearly decreases. Based on these and field observations,  $k_r$  was finally set at 1.25 ( $r_c = 50$  mm).

Figure 8 shows the boundaries of the stress-induced crack zone for different  $b$  values when  $k_r = 1.25$ .

It is clear that at different  $b$  values, the radius of the crack zone around a blast hole differs slightly on the direction of LPTHC, ranging from 1.22 m to 1.36 m. In the direction of  $\sigma_h$ , the crack length is negatively correlated with  $b$ . When  $b = 0$ , the maximum length of radial cracks is 1.75 m. As  $b$  increases, the crack length decreases significantly and reaches the minimum of 0.7 m when  $b = 2.0$ . This suggest that for a given  $\sigma_h$ , increasing  $b$  can suppress crack growth in the direction of  $\sigma_h$  but has little influence on crack propagation along LPTHC.

In the blasting fractured zone, the rock mass is in a low strain rate; the value of which varies with the loading strain

TABLE 2: Rock mechanical parameters.

Density (kg/m <sup>3</sup> )	Elasticity modulus (GPa)	$\mu$	Yield strength (MPa)	Tangent modulus (MPa)	Hardening coefficient	Failure strain	C (s)	P
2450	60	0.25	58.2	61.3	1.25	0.1	2.5	4

TABLE 3: MAT\_ADD\_EROSION parameters.

$mxpres$ (MPa)	$mnpres$ (MPa)	$mxeps$	$mneps$
58.2	-2.6	$2e-3$	$-8e-4$

Note.  $mxpres$ : the maximum hydrostatic pressure should be taken as a positive value, representing pressure. The option is used for controlling the compression failure.  $mnpres$ : contrary to  $mxpres$ , it is used for controlling tensile failure, generally taking negative value.  $mxeps$ : the extreme value of principal strain is used for controlling compression failure, generally taking positive value.  $mneps$ : contrary to  $mxeps$ , it should be taken as a negative value. This option is used for controlling tensile failure.

rate very little. The test results of the static uniaxial tensile strength in the laboratory were 2.6 MPa. Therefore, in the range of loading strain rate on engineering rock blasting, the tensile strength is set to be  $\sigma_{td} = \sigma_t = 2.6$  MPa [32].

In the range of the loading rate of engineering blasting, based on the laboratory test results of the static Poisson ratio for rock mass in Datong Coal Mine Area, according to the mechanical properties of rocks,  $\mu_d = 0.8\mu = 0.2$  [33].  $R_c$  and  $R_p$  were calculated from the parameters given in Table 4 [21] using (1) through (3):  $R_c = 0.15$  m and  $R_p = 1.02$  m. Their sum is 1.17 m, consistent with the numerical result, that is  $(R_c + R_p)_{min} = 1.22$  m. Therefore,  $r_c$  and  $(R_c + R_p)_{min}$  were set to 50 mm and 1.17 m, respectively.

**3.2.2. Secondary Crack Propagation Driven by Detonation Gas.** The number of main cracks in the mathematical model is 4~10 [34], and the rock mass buried underground is broken into five segments with five main cracks after blasting. The number of main cracks is 6~9 under the simulation of different  $k_r$  in Figure 7. Therefore, the number range of the main cracks with quasi-static load exerted by detonating gas is set to be 4~10. After taking into account the connectivity factor between main and wing cracks,  $m$ , the theoretical maximum number of main cracks was calculated at  $n = 10$ . Then, the relationship between  $p_x$  and  $l_{k(max)}$  was obtained for different  $n$  values as shown in Figure 9.

As can be seen from the chart above,  $p_x$  is positively correlated with  $l_{k(max)}$ , and a larger number of main cracks indicate that a higher critical gas pressure is needed for crack propagation. The steady pressure of detonation gas present in initial cracks was calculated at 79 MPa using (6) and (8). When  $n = 8$  and 10,  $l_{k(max)}$  is 0.62 m and 0.26 m, respectively. Therefore, the maximum length of secondary cracks was  $l_{k(max)} = 0.26$  m ( $n = 10$ ).

**3.2.3. Length of Cracks Guided by Empty Holes.** Based on the numerical calculation model of blasting hole spacing 3.2 m, the evolution characteristics of the rock element tangential peak stress in different positions along the LPTHC are compared and analyzed between the conventional rock and

the rock with empty hole. The distances from observation points A, B, C, and D to the empty-holes center nearby are 0.05 m, 0.15 m, 0.25 m, and 0.35 m, respectively, and the stress concentration effect of the empty hole with numerical simulation is obtained shown in Figure 10.

The tangential stress peaks at the observation points A, B, and C in the case with empty holes increase 96.2%, 55.6%, and 14.3%, respectively, compared to those in the case without empty holes. However, at point D does not differ between the two cases. This suggests that the presence of empty holes causes tangential stress concentration along the LPTHC. Thus, this line becomes the dominant orientation of empty hole-guided cracks, and a weak plane between holes is likely to develop along it.

Figure 11 shows the theoretical and simulated relationships between  $l_{t(max)}$  and  $r_k$  (0.025 m, 0.03 m, 0.041 m, 0.05 m, 0.06 m, 0.07 m, 0.08 m, 0.12 m, and 0.2 m), which were obtained by (10) and curve fitting, respectively.

The simulated  $l_{t(max)}$  has an inflection point at  $r_k = 0.05$  m, and the calculated  $l_{t(max)}$  has an inflection point at  $r_k = 0.1$  m. When  $r_k \leq 0.05$  m, the simulated  $l_{t(max)}$  increases rapidly with increasing  $r_k$ , and the rate of increase is 53.9%, as indicated by the first portion ( $r_k = 0.03$  m~0.05 m, Stage I) of the corresponding curve. When  $r_k > 0.05$  m, the cumulative increase in the simulated  $l_{t(max)}$  is small at 0.04 m with  $l_{t(max)}(r = 0.05 \text{ m}) = l_{t(max)}(r = 0.06 \text{ m})$ , as demonstrated by the second portion of the simulated curve (Stage II). The first portion of the calculated curve ( $r_k \leq 0.1$  m) is approximately horizontal. When  $r_k > 0.1$  m, the calculated value of  $l_{t(max)}$  tends to increase linearly with increasing  $r_k$ . The second portion of the calculated curve slopes more steeply than the corresponding part of the simulated curve.  $l_{t(max)}$  is positively correlated with  $r_k$  overall. However, increasing  $r_k$  will also substantially increase the amount of drilling. So, the optimal value for  $r_k$  should be 0.05 m, and the corresponding  $l_{t(max)}$  is 0.21 m.

Then  $L = 2l_0 = 2(R_c + R_p + l_{k(max)} + l_{t(max)}) = 2 \times (1.17 + 0.26 + 0.21) = 3.28$  m. Therefore, the optimal distance from an empty hole to an adjacent blast hole was set at 1.6 m and the optimal blast-hole spacing was 3.2 m.

**3.3. Numerical Results and Analysis.** Numerical simulation using a deep-hole blast model with  $L = 3.2$  m (shown in Figure 12) was performed to monitor the dynamics of equivalent stress and strain and expound crack evolution along the LPTHC.

**3.3.1. Dynamics of Equivalent Stress at a Cross Section.** Figure 13 shows the fringe pattern of equivalent stress at a cross section after blasting. Figure 14 illustrates the dynamics of equivalent stress in rock elements.

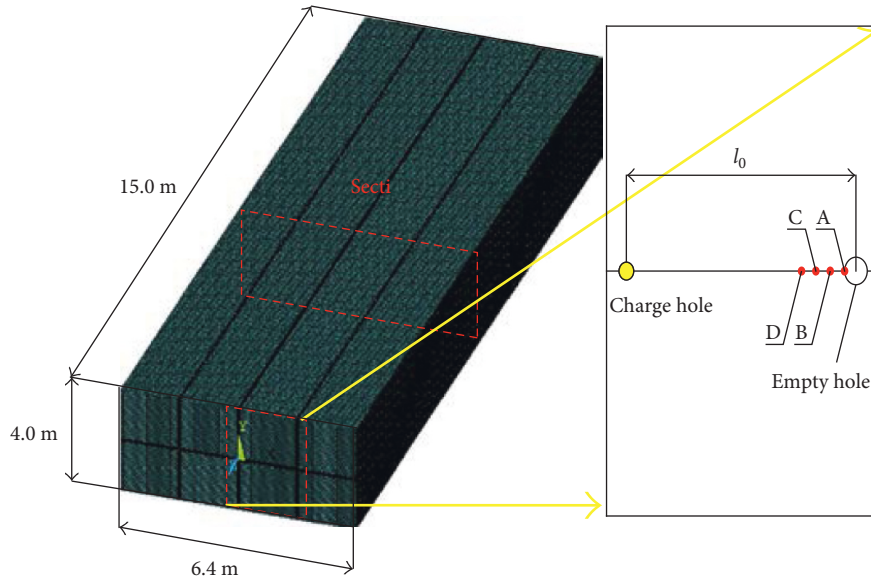


FIGURE 5: Model boundary and layout of observation points.

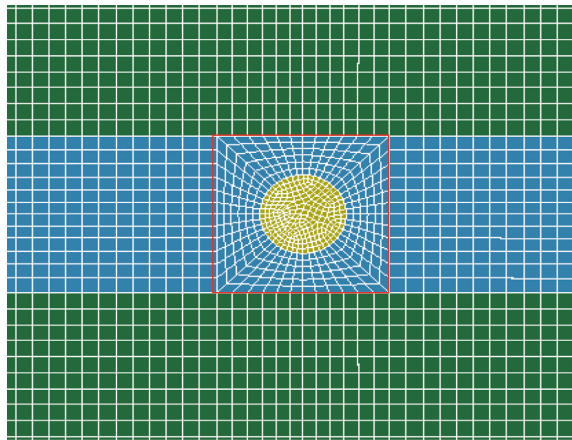


FIGURE 6: Larger image of grid around the blasting hole.

Figure 13(a) shows the crushed zone and fractured zone created by stress waves around a blast hole. Meanwhile, the stress wave propagation is concentric circles distribution with a blasting hole as a center, and the equivalent stress peak near the blasting hole reaches 45.0 MPa. Figure 13(b) demonstrates that  $t = 199.2 \mu\text{s}$  the stress wave of two adjacent blasting holes is superimposed around the empty hole, and the tangential stress concentration effect is further strengthened. Then, the rock is fractured along the LPTHC in the near of empty holes. With the transmission of the blasting stress, the length of the stress concentration area in the near of empty holes is increased to the maximum 0.38 m when  $t = 552.5 \mu\text{s}$ , but the tensile length induced by the reflected tensile stress reaches 0.21 m, which is connected with the secondary fracture driven by detonation gas. It showed that the crack induced by the tensile stress is synchronous with the secondary fracture driven by detonation gas; that is, the blasting stress wave propagates ahead of the crack propagation. In Figures 13(b)–13(d), the tangential

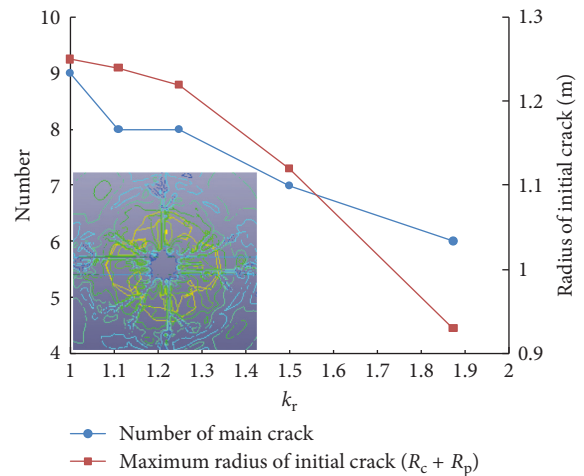


FIGURE 7: Effects of  $k_r$  on the development of main cracks.

peak stress is all in the vicinity of fractured zone around empty hole, which is employed LPTHC as a center symmetry axis. The results show the stress concentration effect of the empty hole, especially obvious on the LPTHC.

Figure 14 reveals that the stresses in different elements follow the same trend overall, but the peak values differ and occur at different times. Stress propagation consists of two major stages: propagation of stress wave generated by blasting (Stage I) and reflected tensile wave (Stage II). Thus the stress in each element has two extreme values. At Stage I, the peak stress at each observation point firstly decreases sharply and then decreases slightly, and a stress wave reaches point D at 0.2 ms. Stress-induced fracturing and stress wave propagation take place simultaneously. Later, the crack growth driven by detonation gas stops at a point located between points C and D, which is consistent with the peak stress trend predicted by (3), (8), and (10). After stress spreads into Stage II at 0.39 ms, the tensile wave reflected



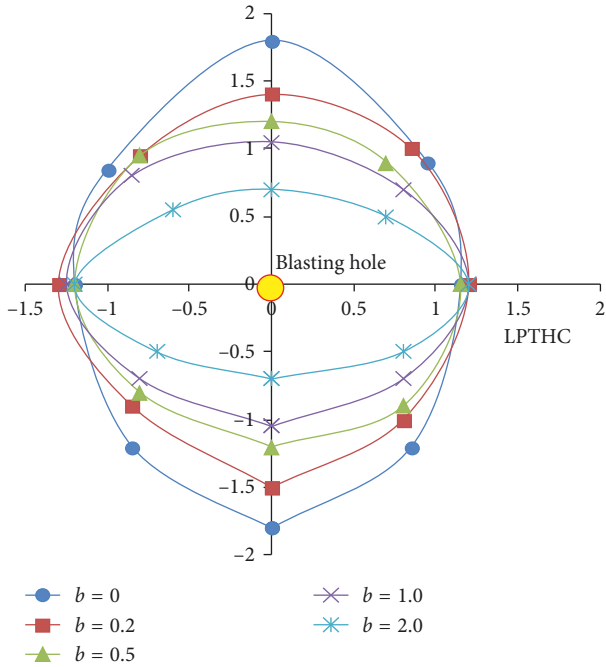


FIGURE 8: Boundary of the stress-induced crack zone around a blasting hole.

TABLE 4: Explosion calculating parameters for rock.

$\rho$ (kg/m <sup>3</sup> )	$D_p$ (m/s)	$\mu$	$\mu_d$	$b$	$\sigma_c$ (MPa)	$\xi$	$\sigma_h$ (MPa)
2450	5650	0.25	0.2	1/4	58.2	1000	6.0

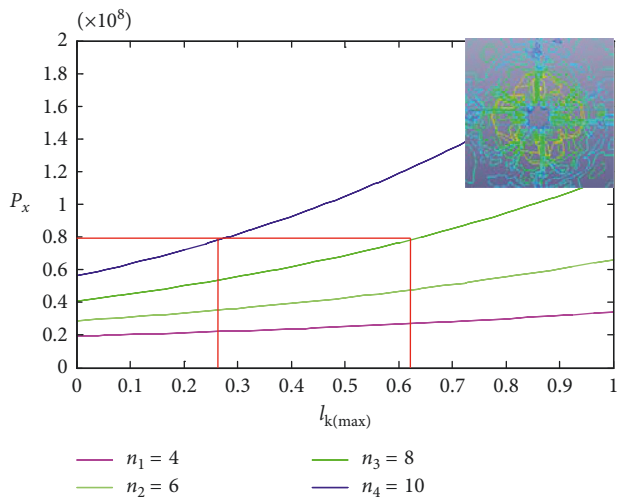


FIGURE 9: Effect of expanding medium pressure on crack development.

from free surfaces around point A needed for fracture strength results in rock cracking. As stress propagation continues, stress wave passes points B and C for the second time. The resulting stress peak at point C (13.0 MPa) is a bit lower than that at point B, and both meet the fracture

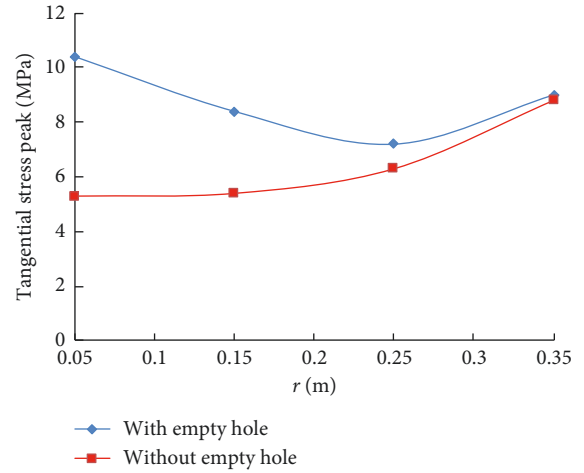


FIGURE 10: Empty-hole effect during stress wave propagation.

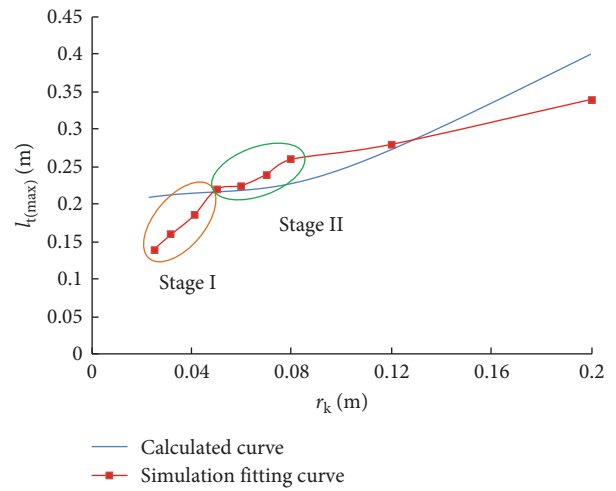


FIGURE 11: Variation in  $I_{t(max)}$  with  $r_k$ .

criterion given by (10). Thus cracks initiate at the two locations. As stress wave propagates to point D for the second time, the stress there peaks at a significantly higher level (increasing amplitude 5.0 MPa). This is because this stress peak is a complex tensile stress arising from a combination of the reflected tensile wave and the quasi-static stress produced by detonation gas. It can drive wing cracks to further propagate and connect with main cracks into an intensive fracture network.

3.3.2. *Characteristics of Strain around the Empty Hole and Blast-Induced Crack Evolution.* The effect of holes' spacing (2.7 m, 3.2 m, and 3.7 m) on the strain in elements along the LPTHC was analyzed using the deep-hole blast model with empty holes. The characteristics of main and wing cracks' evolution in the section under analysis confirm the reasonableness of the hole spacing determined.

Figure 15 depicts the variation in the strain of the element at the empty hole's free surface for different hole spacing.

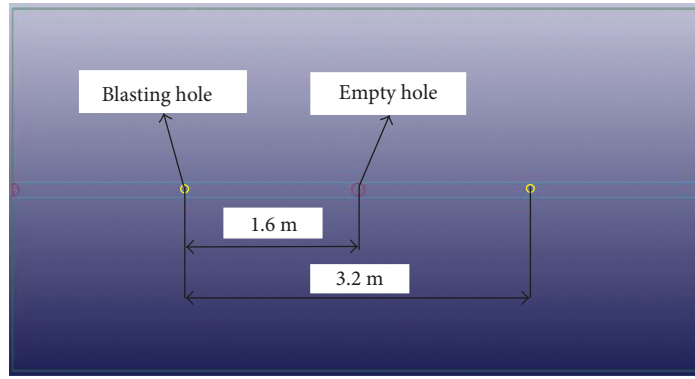


FIGURE 12: Boreholes layout.

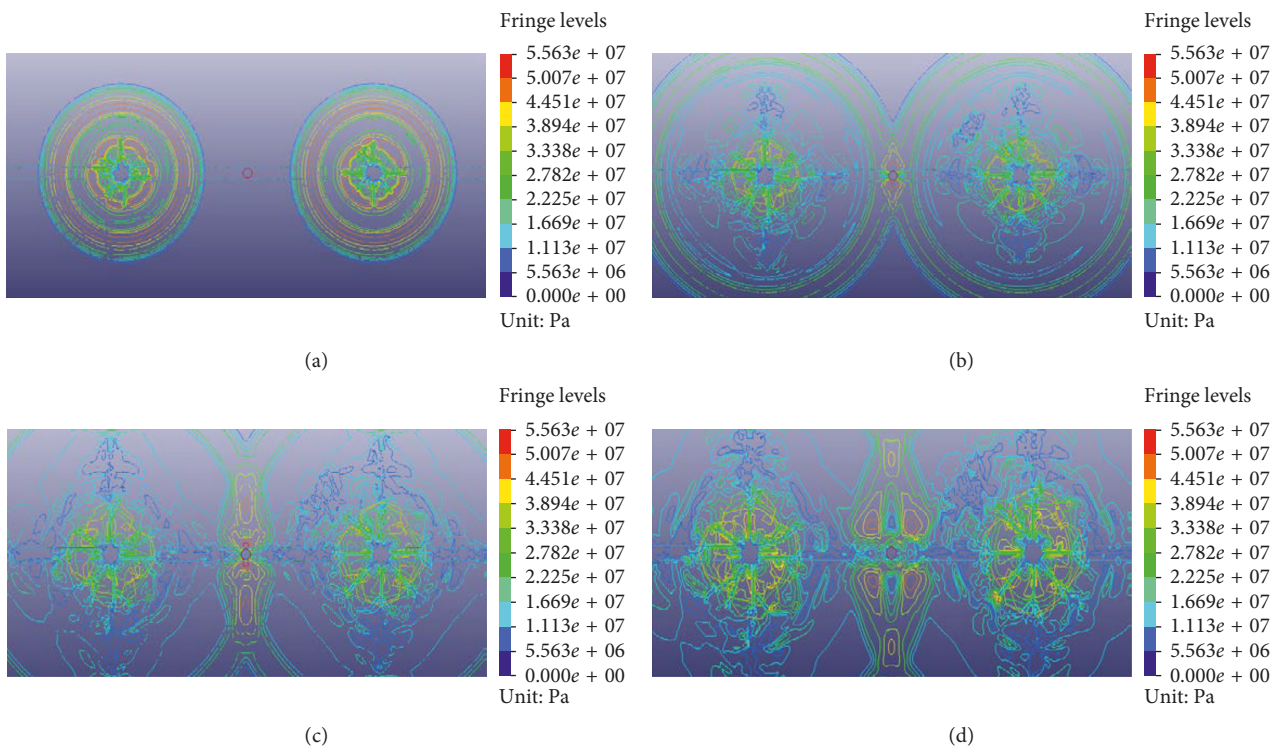


FIGURE 13: Fringe patterns of equivalent stress. (a) 109.3 μs. (b) 199.2 μs. (c) 449.8 μs. (d) 552.5 μs.

The compressive strain and tensile strain in the rock elements follow the same downward trend. The compressive strain caused by blasting is instantaneously converted to tensile strain at the free surface. As the hole spacing increases, the strain peak in the peripheral element decreases linearly. When the hole spacing is greater than 3.7 m, the dynamic tensile strain peak is slightly higher than the experimental critical value, which will impede failure of elements distant from the empty holes.

Figure 16 shows the variation of strains' peak along the LPTHG under different holes' spacing.

As reflected tensile wave propagates, the elements along the LPTHG undergo tensile strain. The tensile strain peak has a negative correlation with  $r$  and varies nearly linearly with it. When  $L = 3.7$  m, 3.2 m, and 2.7 m, the critical values

of  $r$  needed for failure are 0.27 m, 0.25 m, and 0.15 m, respectively. The corresponding rates of decrease are 7.4% and 66.7%, suggesting that an increase in  $L$  is associated with more significant decrease in tensile strain peak with  $r$ . This, together with the strain variation with hole spacing change, demonstrates that the hole spacing of 3.2 m can allow reflected stress waves to effectively cause tensile failure and promote fracturing guided by the empty holes. Moreover, this hole spacing does not require a large amount of drilling.

The characteristic zones of main and wing cracks across a section were identified through crack evolution simulation with  $L = 3.2$  m, as shown in Figure 17. The yellow zone boundary is the crack tip connection of the detonation products expansion.

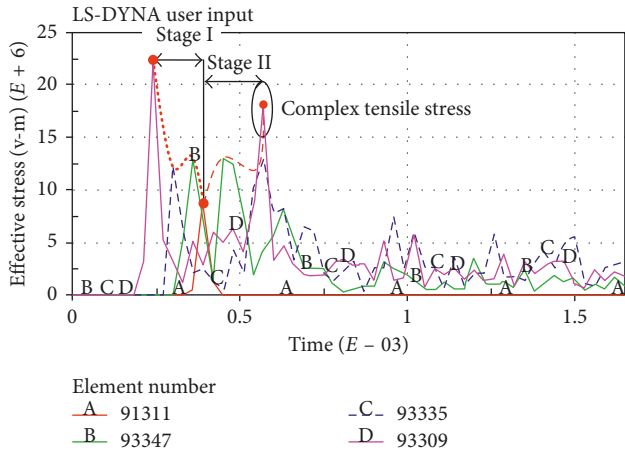


FIGURE 14: Evolution law of the rock element equivalent stress.

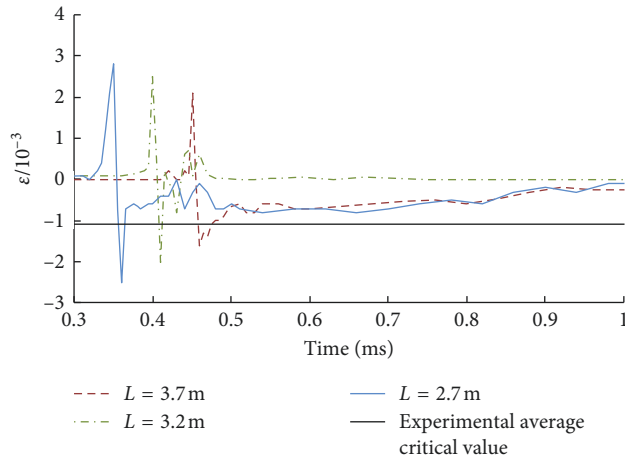


FIGURE 15: Strain evolution around the free surface of the empty hole. Note that Compression strain is positive and tension strain is negative.

Figure 18 reveals the temporal evolution on the range of main cracks along the LPTHC and the boundaries between different crack zones.

Figure 17 shows that, in the initial stage of blasting, a crushed zone was formed with a radius of 0.13 m, shown in Figure 17(a). When  $t = 196.2 \mu\text{s}$ , the crack zone around a blast hole had a radius of 0.44 m, and the detonation gas spread over 0.28 m in the rock. At  $341.5 \mu\text{s}$ , the crack zone's radius was 0.79 m and the distance traveled by the detonation gas was 0.61 m, which implies that the fracturing driven by detonation gas far lagged behind stress waves. At  $490.1 \mu\text{s}$ , the diffusion distance of detonation gas was 0.88 m from the blasting hole, and meanwhile, the stress wave fracturing reaches the maximum,  $R_c + R_p = 1.15 \text{ m}$ . After this, the detonation gas induces secondary propagation of initial cracks, and both are synchronized. At  $681.3 \mu\text{s}$ , the tensile cracks induced by stress waves reflected from the empty hole's surface interconnected with the secondary cracks induced by detonation gas. At this point, the maximum radius of the crack zone around an empty hole was

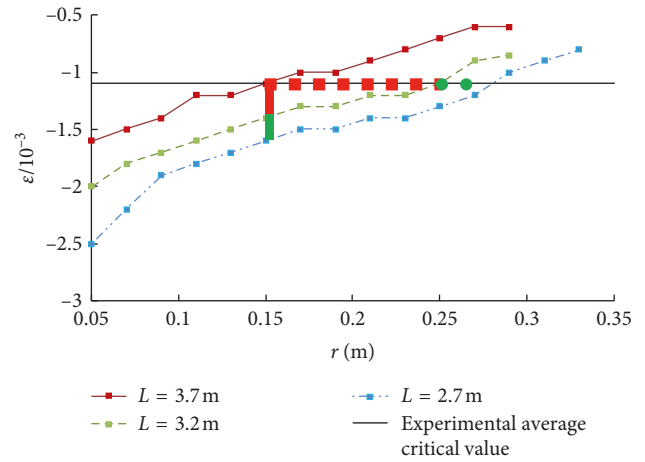


FIGURE 16: Strains' peak curve for different holes' spacing along the LPTHC.

0.21 m. Meanwhile, the accumulated fracturing length driven by detonating gas was  $l_{k(\text{max})} = 0.24 \text{ m}$ . Therefore, the accumulated lengths of the crushed zone and initial crack zone were 1.15 m, the secondary crack zone was 0.24 m long, and the crack zone around the empty hole was 0.21 m long (Figure 18). These are roughly consistent with the results of fitting, thus confirming the reasonableness of the holes' spacing determined, at 3.2 m.

The zones indicated by the ovals shown in Figure 17(d) contain high densities of wing cracks induced by lagged stress waves. This is because the quasi-static stress field in the rock mass created by the detonation gas, together with the flow of detonation gas into the wing cracks connecting to main cracks, promoted further expansion of main cracks and development of circumferential wing cracks. Figure 17(e) reveals that the main cracks and wing cracks interconnected into an "F"-shaped fracture network after the blasted rock mass reached a stable state. It follows that the hole spacing, 3.2 m, determined allows the main and wing cracks between holes to interconnect efficiently and thereby ensures effective presplitting.

#### 4. Application to a Project

**4.1. Project Background.** The 8939 working face at Xinzhouyao Mine in Datong Coal Mine Area has an average burial depth of 311.4 m and a length of 104.5 m. The coal seam, with the dip angle of  $3^\circ$  on average, is characterized by uniform coal properties, stable distribution, and simple structure. ZZ9900/29.5/50 hydraulic supports are used at the face. Figure 19 shows local stratigraphic characteristics.

The hard main roof of the face is composed of 15.7 m thick medium sandstone. With no joints and high structural stability, the main roof does not fall readily as the face advances. Long suspended roof behind the face can increase the possibility of strong strata behavior, posing a serious threat to mine safety. For this reason, deep-hole blasting aided by empty holes was performed to presplit the main roof. It was

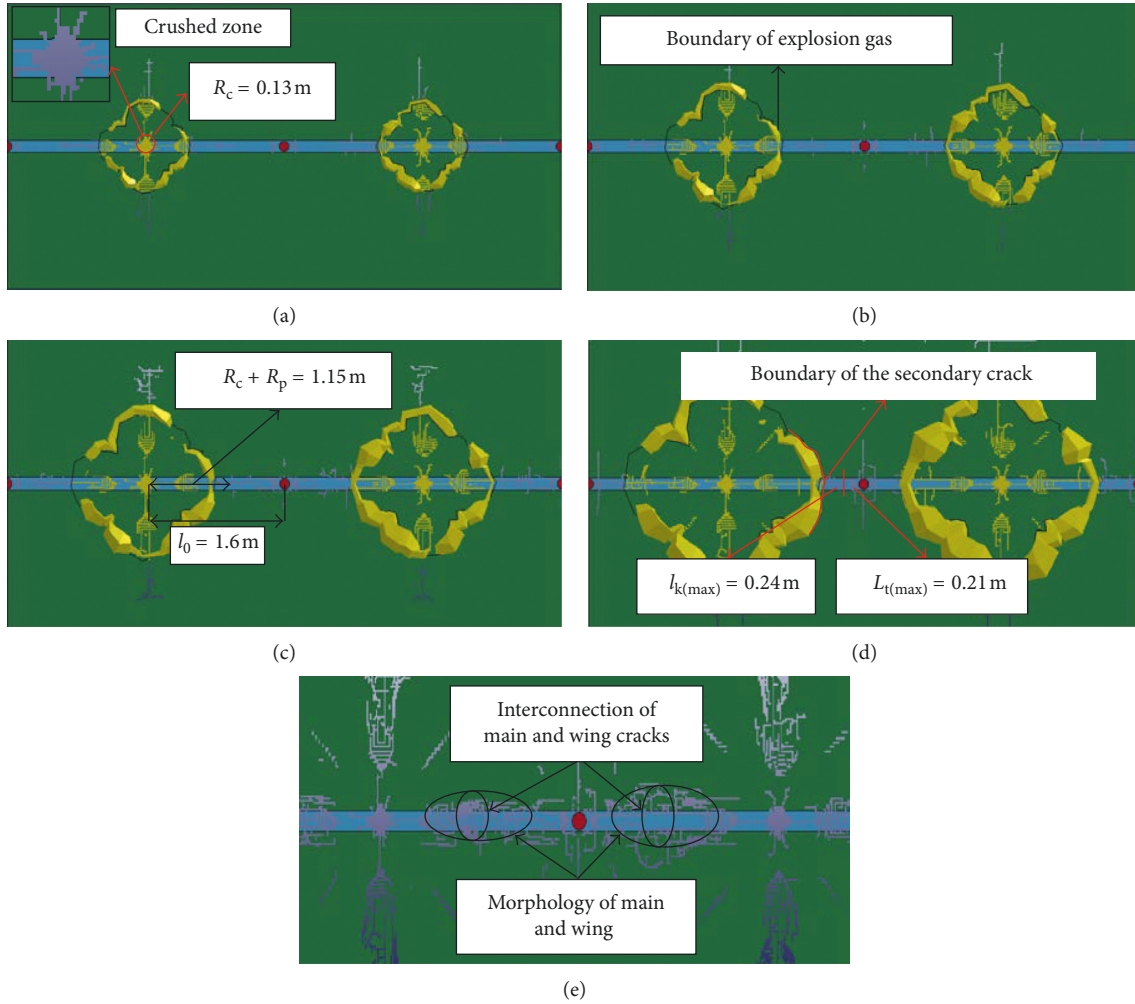


FIGURE 17: Evolution law of fracture field. (a) 196.2  $\mu\text{s}$ . (b) 341.5  $\mu\text{s}$ . (c) 490.1  $\mu\text{s}$ . (d) 681.3  $\mu\text{s}$ . (e) 953.7  $\mu\text{s}$ .

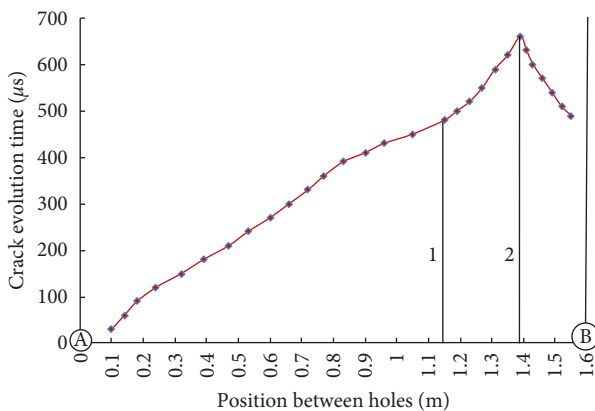


FIGURE 18: Variation in crack length with time. A is the blasting hole; B is the empty hole; line 1 indicates the boundary between initial crack zone and secondary crack zone; line 2 represents the position where secondary cracks meet the tensile cracks induced by reflected stress waves.

expected to create vertical and interlayer weak planes, reduce the sizes of caved rock blocks, mitigate the intensity of strata behavior, and thereby enhance mine safety.

4.2. *Presplit Blasting Scheme.* Based on the  $k_r$  analysis presented above, the diameters of blast holes and empty holes were designed to be 50 mm and 100 mm. Each empty-hole group was 1.6 m from adjacent blast-hole groups. The holes drilled at the same height were within the same plane, and the lower roadside holes were 1.2 m from the floor. The blast holes for detonation should be at least 30 m ahead of the face. The last holes group was located 30 m from the terminal line.

After drilling, explosive charges were loaded into the blast holes, with the detonator placed to each hole bottom. The detonating cord was bundled to the first charge, and the blast holes were connected in series. Figure 20 shows the profile of each blast-hole group, and structural parameters of charge are shown in Table 5.

4.3. *Analysis on the Field Effect*

4.3.1. *Fracture Propagation of Empty Holes before and after Blasting.* For the length of the deep hole sealing, with the hole being 14.0 m, considering the equipment limited and avoiding being trapped in the hole, the borehole camera was employed for monitoring the development of fractures in


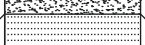






Jurassic	Buried depth (m)	Columnnar	Min~max average thickness (m)	Lithology
	276.4		$\frac{0.2\sim 0.8}{0.4}$	10# coal
	279.9		$\frac{3.2\sim 3.7}{3.5}$	Siltstone
	291.5		$\frac{6.5\sim 16.7}{11.6}$	Fine sandstone
	295.7		$\frac{3.5\sim 4.7}{4.2}$	Gritstone
	311.4		$\frac{14.0\sim 17.5}{15.7}$	Medium sandstone
	314.1		$\frac{2.1\sim 3.3}{2.7}$	Finestone
	321.5		$\frac{5.2\sim 9.1}{7.4}$	11#~12# coal
	324.9		$\frac{1.7\sim 5.1}{3.4}$	Finestone

FIGURE 19: Local stratigraphic characteristics.

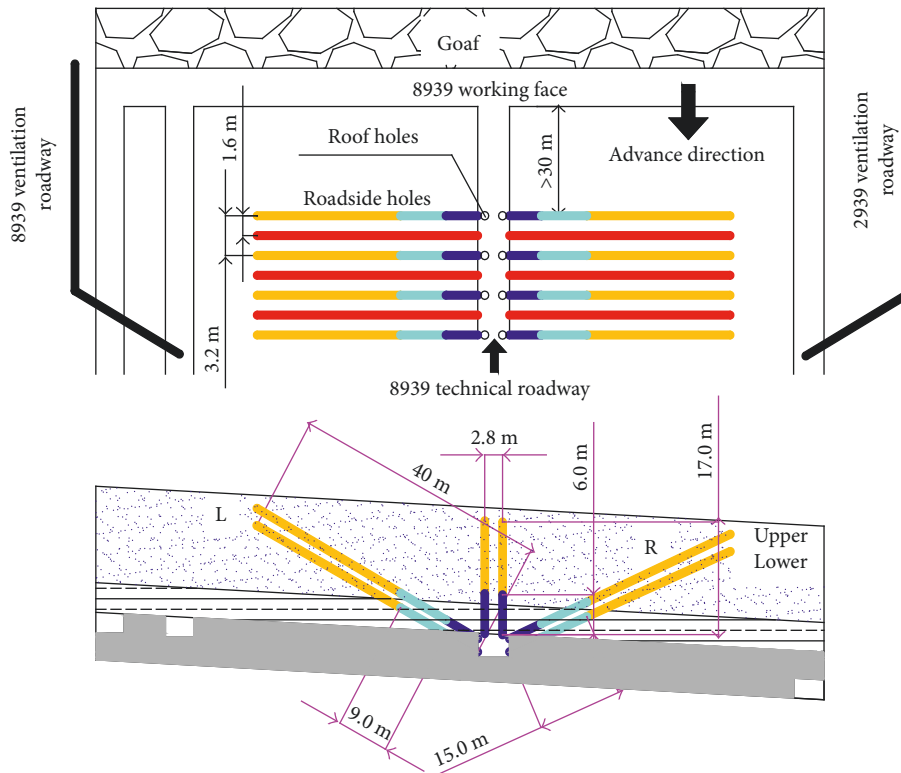


FIGURE 20: Presplitting blasting profile of each blast-hole group.

the hole depths of 18.0 m~22.0 m before and after blasting. The deep-hole blasting presplitting was implemented ahead of the coal wall 32.0 m. The fracture images of the holes' wall are presented in Figure 21 before blasting, in which the local holes' wall was fractured discontinuously with a maximum aperture of 3.0 mm (yellow circles shown in Figures 21 and 22).

After blasting, the secondary crack developed violently and the surrounding rock was seriously damaged. Blasted fracture developed along the whole borehole axial length, with the maximum opening reaching 15 mm, as shown in Figure 22 (red line). In the borehole screenshots, when the depth was 18.0 m, the borehole fracture was densely

TABLE 5: Charge parameters of blast holes.

Holes	Hole depth (m)	Elevation (°)	Vertical height (m)		Sealing length (m)	Sealing material		Charge weight (kg)
			Upper	Lower				
Roadside	L	40.0	29	22.5	14	9 m stemming	6 m expansive cement	36
	R	38.2	24	18.6	14	9 m stemming	6 m expansive cement	24
Roof		17.0	90	18.0	6	6 m stemming		16.5

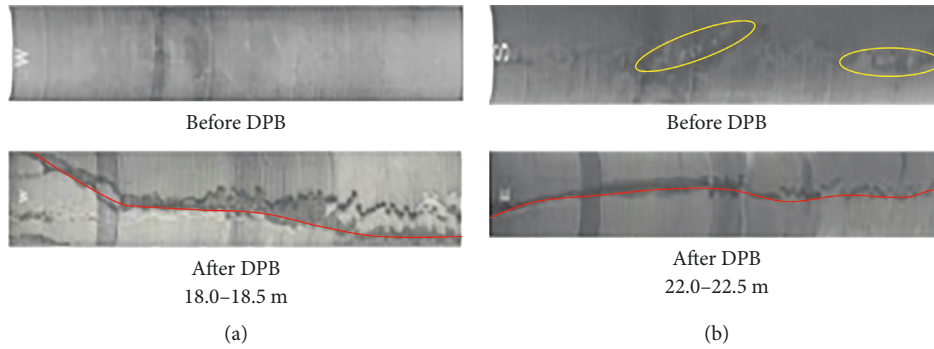


FIGURE 21: Fracture variation along the holes axis before and after blasting. (a) 18.0–18.5 m. (b) 22.0–22.5 m.

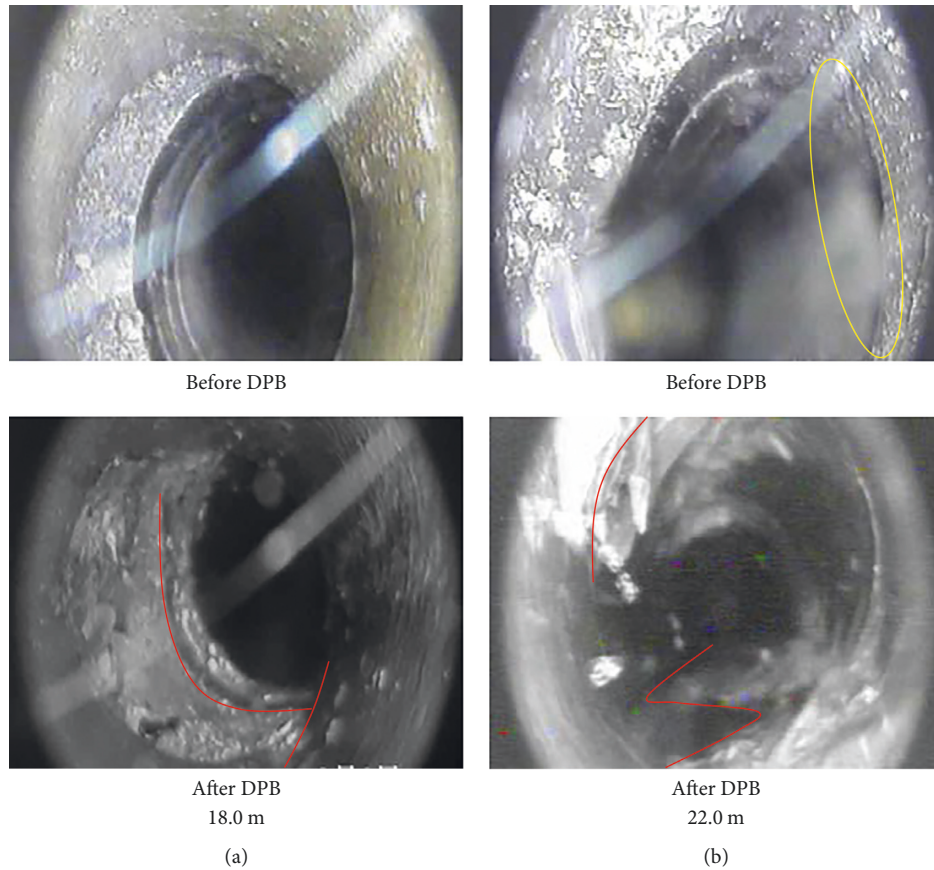


FIGURE 22: Typical screenshots at different holes depth before and after DPB. (a) 18.0 m. (b) 22.0 m.

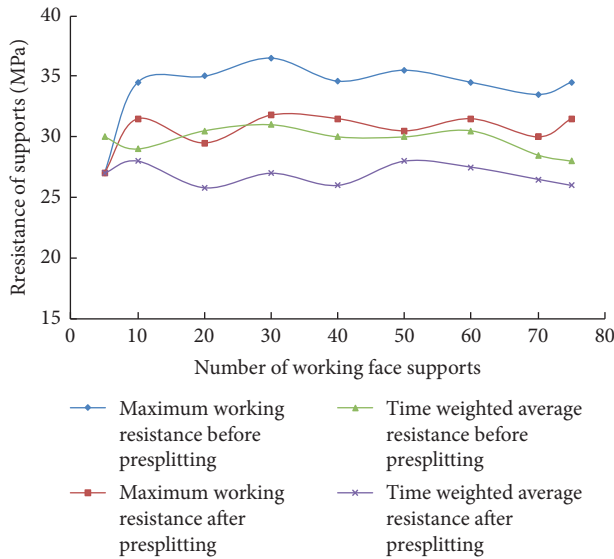


FIGURE 23: Comparison on working resistance of support before and after presplitting.

developed and broken in the whole section. At the depth of 22.0 m, the hole wall was seriously fragmented and the diameter decreased to about 1/2 of that before blasting. It shows the guiding and presplitting effect of the empty hole; that is, the deep-hole presplitting blasting could produce significant cracks around empty holes.

4.3.2. *Strata Behavior of Working Face before and after Presplitting.* Figure 23 illustrates the variation in the working resistance of the face supports before and after presplitting.

A comparison of the working resistance before and after presplitting suggests that the maximum working resistance of the middle support decreased 15% from 36.2 MPa to 30.8 MPa. The corresponding time weighted average resistance decreased 16% from 31 MPa to 26 MPa. Besides, the unsupported roof near the location of presplitting did not fall in the forms of roof leakage and rock mass with cutting and breaking, demonstrating that the blasting produced good results and enhanced safety at the face.

## 5. Conclusions

- (1) In presplit blasting, rock fracturing is the product of the synergistic action of stress waves and detonation gas. The study found that the presence of empty holes between blast holes can improve tangential stress distribution and guide crack propagation. The characteristic zones of crack initiation, propagation, and interconnection were identified.
- (2) The radius of the crack zone around a blast hole and the length of secondary cracks induced by detonation gas were derived. The maximum length of cracks guided by empty holes along the LPTHG was analyzed with respect to rock stress.

- (3) The lengths of the secondary crack zone for different numbers of main cracks near a blast hole were determined. The effects of  $k_r$  and  $r_k$  on the range of blast-induced cracks were analyzed. Based on the results, the optimal spacing between blast hole and empty hole was set at 1.6 m.
- (4) The mechanism of crack propagation between holes was revealed through analysis on evolution of equivalent stress distribution, strain variation, and partition evolution of main cracks and wing cracks. The interconnectivity of main cracks and wing cracks demonstrates that the rock between holes was successfully prefractured.
- (5) A plan for implementing deep-hole blasting to presplit thick and hard rock mass was designed and applied in 8939 working face of Xinzhouyao Mine, and field measurement suggests that the split blasting technique led kerf and weaken plane to the rock mass with a significant decrease of working resistance of support and strata behaviors.

## Data Availability

The data used to support the findings of this study are available from the corresponding author upon request.

## Conflicts of Interest

The authors declare that there are no conflicts of interest regarding the publication of this paper.

## Acknowledgments

This work was supported by the National Natural Science Foundation of China (No. 51604262 and 51574220), the Research and Innovation Project for College Graduates of Jiangsu Province (Grant No. KYLX16\_0558), and the Fundamental Research Funds for the Central Universities of China University of Mining and Technology (No. 2014ZDPY21).

## References

- [1] J. X. Yang, C. Y. Liu, and B. Yu, "Application of confined blasting in water-filled deep holes to control strong rock pressure in hard rock mines," *Energies*, vol. 10, no. 11, p. 1874, 2017.
- [2] W. L. Fournery, J. W. Dally, and D. C. Holloway, "Controlled blasting with ligamented charge holders," *International Journal of Rock Mechanics and Mining Sciences*, vol. 15, no. 3, pp. 121–129, 1978.
- [3] B. B. Mohanty, "Explosion generated fracture in rock and rock like materials," *Engineering Fracture Mechanics*, vol. 35, no. 4–5, pp. 889–898, 1990.
- [4] Z. W. Yue, L. Y. Yang, and Y. B. Wang, "Experimental study of crack propagation in polymethyl methacrylate material with double holes under the directional controlled blasting," *Fatigue and Fracture of Engineering Materials and Structures*, vol. 36, no. 8, pp. 827–833, 2013.
- [5] K. F. Bian, H. B. Li, and Y. Q. Liu, "Numerical simulation for the damping effect of empty holes on blasting vibration," *Advanced Materials Research*, vol. 936, pp. 1490–1495, 2014.

- [6] S. C. Zhou, D. Li, F. W. Zhang et al., "Optimization analysis of drilling layout based on blasting releasing pressure and its application," *Chinese Journal of Rock Mechanics and Engineering*, vol. 32, pp. 807–813, 2013.
- [7] K. Nakagawa, T. Sakamoto, and R. Yoshikai, "Model study of the guide hole effect on the smooth blasting," *Journal Japan Explosives Society*, vol. 43, pp. 75–82, 1982.
- [8] Y. Chen, S. P. Hao, Y. T. Chen et al., "Study on the application of short-hole blasting with guide hole to roof cutting pressure relief of gob-side entry retaining," *Journal of Mining and Safety Engineering*, vol. 32, pp. 253–259, 2015.
- [9] K. Arkawa and T. Mada, "Unsteady dynamic crack propagation in a brittle polymer," *Experimental Mechanics*, vol. 47, no. 5, pp. 609–615, 2007.
- [10] Z. L. Wang and H. Konietzky, "Modeling of blast-induced fractures in jointed rock masses," *Engineering Fracture Mechanics*, vol. 76, no. 12, pp. 1945–1955, 2009.
- [11] R. S. Yang, C. Chen, X. Wang et al., "Experimental investigation on the influence of different diameter empty holes on the crack growth behavior of blasting," *Journal of China Coal Society*, vol. 42, pp. 2498–2503, 2017.
- [12] R. S. Yang, Y. L. Che, X. Tong, Y. L. Mi, and L. Feng, "Experimental study on the technology of middle empty hole in parallel hole cut blasting," *Advanced Materials Research*, vol. 594–597, pp. 1314–1317, 2012.
- [13] M. P. Malezhik, O. P. Malezhik, and I. Chernyshenko, "Photoelastic determination of dynamic crack-tip stresses in an anisotropic plate," *International Applied Mechanics*, vol. 42, no. 5, pp. 574–581, 2006.
- [14] Z. W. Yue, Y. Guo, X. Wang et al., "Influence of empty hole shape on directional fracture controlled blasting of rock," *Rock and Soil Mechanics*, vol. 37, pp. 376–382, 2016.
- [15] R. Yang and Y. Wang, "Experimental research on the influence of an empty-hole defect on crack connections between a directionally fractured blast hole," *Journal of Testing and Evaluation*, vol. 45, no. 6, pp. 2139–2150, 2017.
- [16] S. H. Cho, Y. Nakamura, B. B. Mohanty, H. S. Yang, and K. Kaneko, "Numerical study of fracture plane control in laboratory-scale blasting," *Engineering Fracture Mechanics*, vol. 75, no. 13, pp. 3966–3984, 2008.
- [17] Y. Nakamura, S. H. Cho, M. Yoneoka et al., "Model experiments on crack propagation between two charge holes in blasting," *Science and Technology of Energetic Materials*, vol. 65, pp. 34–39, 2004.
- [18] W. Lu, Z. Leng, M. Chen et al., "A modified model to calculate the size of the crushed zone around a blast-hole," *Southern African Institute of Mining and Metallurgy*, vol. 116, no. 5, pp. 413–422, 2016.
- [19] R. Yang, W. F. Bawdens, and P. D. Katsabaniss, "A new constitutive model for blast damage," *International Journal of Rock Mechanics and Mining Sciences*, vol. 33, no. 3, pp. 245–254, 1996.
- [20] J. Dai, "Calculation of radii of the broken and cracked areas in rock by a long charge explosion," *Journal of Liaoning Technical University Natural Science Edition*, vol. 20, pp. 144–147, 2001.
- [21] J. Dai, *Rock Dynamic Characteristics and Blasting Theory*, Press of Metallurgy Industry, Beijing, China, 2002.
- [22] L. F. Trivino and B. Mohanty, "Assessment of crack initiation and propagation in rock from explosion-induced stress waves and gas expansion by cross-hole seismometry and FEM–DEM method," *International Journal of Rock Mechanics and Mining Sciences*, vol. 77, pp. 287–299, 2015.
- [23] X. L. Yang and M. S. Wang, "Mechanism of rock crack growth under detonation gas loading," *Explosion and Shock Waves*, vol. 21, pp. 111–116, 2001.
- [24] S. L. Liu, W. P. Li, and Q. Q. Wang, "Numerical simulation on crack propagation of rock mass with a single crack under seepage water pressure," *Advances in Mechanical Engineering*, vol. 9, no. 10, pp. 1–12, 2017.
- [25] T. Y. Fan, *Principle and Application of Fracture Mechanics*, Press of Beijing Institute of Technology, Beijing, China, 2006.
- [26] S. Zhang and Q. Z. Wang, "Determination of rock fracture toughness by split test using five types of disc specimens," *Rock and Soil Mechanics*, vol. 30, pp. 12–18, 2009.
- [27] J. S. Sun, C. Q. Zuo, C. B. Zhou et al., "Dynamic disturbing on a round tunnel subjected to blasting seismic wave," *Journal of Vibration and Shock*, vol. 34, pp. 7–12, 2015.
- [28] Z. L. Xu, *Elasticity Mechanics*, Higher Education Press, Beijing, China, 2013.
- [29] H. B. Li, X. Xia, J. C. Li, Z. Jian, L. Bo, and L. Yaqu, "Rock damage control in bedrock blasting excavation for a nuclear power plant," *International Journal of Rock Mechanics and Mining Sciences*, vol. 48, no. 2, pp. 210–218, 2011.
- [30] E. L. Lee and C. M. Tarver, "Phenomenological model of shock initiation in heterogeneous explosives," *Physics of Fluids*, vol. 23, no. 12, pp. 2362–2372, 1980.
- [31] Livermore Software Technology Corporation, *LS-DYNA Keyword User's Manual*, LSTC, Livermore, CA, USA, 2003.
- [32] S. L. Yan and Y. Xu, "Numerical simulation of water-coupled charge rock blasting mechanism," *Chinese Journal of Underground Space and Engineering*, vol. 1, pp. 921–924, 2005.
- [33] P. Segarra, A. Sanchidrian, R. Castedo, and I. del Castillo, "Coupling of blasting seismographs to rock and its effectiveness for horizontal ground motion," *International Journal of Rock Mechanics and Mining Sciences*, vol. 92, pp. 81–90, 2017.
- [34] R. K. Garnsworthy, "The mathematical modeling of rock fragmentation by high pressure arc discharges," in *Proceedings of the 3rd International Symposium on Rock Fragmentation by Blasting*, pp. 143–147, Brisbane, Australia, 1990.





**Hindawi**

Submit your manuscripts at  
[www.hindawi.com](http://www.hindawi.com)

